

Crystal Shape Tailoring in Perovskite Structure Rare-Earth Ferrites REFeO₃ (RE = La, Pr, Sm, Dy, Er, and Y) and Shape-Dependent Magnetic Properties of YFeO₃

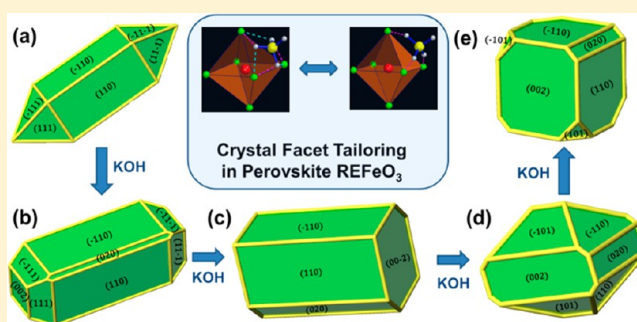
Long Yuan,^{†,§} Keke Huang,[†] Shan Wang,[‡] Changmin Hou,[†] Xiaofeng Wu,[†] Bo Zou,[§] and Shouhua Feng^{*,†}

[†]State Key Laboratory of Inorganic Synthesis and Preparative Chemistry, College of Chemistry and [§]State Key Laboratory of Superhard Materials, Jilin University, Changchun 130012, P. R. China

[‡]Department of Materials Science and Engineering, Jilin Institute of Chemical Technology, 45 Chengde Street, Jilin 132022, P. R. China

S Supporting Information

ABSTRACT: Controllable growth of perovskite oxide with tailored shapes is challenging but promising for shape-dependent physical and chemical property studies and probable applications. In this article, we report a general method for tailoring the crystal shape of perovskite structure rare-earth ferrite (REFeO₃) crystals in hydrothermal conditions. By adjusting the ratio of KOH to urea, various shapes of REFeO₃ crystals can be prepared, such as LaFeO₃ truncated cubes, PrFeO₃ perpendicular cross prisms, SmFeO₃ crossed bars with trustum, DyFeO₃ double pyramids on cubes, ErFeO₃ distorted octahedrons, and YFeO₃ long bars and thick hexagonal elongated plates. Detailed shape tailoring conditions for each phase of the crystals have been discussed clearly. The structure-dependent shape growing mechanism for each REFeO₃ is generally discussed by consideration of the variance of reduced unit cell parameters in reference to the ideal cubic ABO₃ perovskite structure. DyFeO₃ was taken as an example to elucidate the crystal shape formation mechanism based on the Bravais–Friedel–Donnay–Harker theory. The magnetic property of the YFeO₃ crystal shows shape dependence: elongated bars have the highest saturated magnetization, while the lowest coercive field, while the tailored polyhedrons are vice versa. This paper not only builds a general technique for tailoring the crystal shape to various shapes of REFeO₃ crystals but also provides many crystals for further study and application of anisotropy either in physical or in chemical properties.



INTRODUCTION

Crystals with different shapes are usually grown with different facets, which provide a platform to study the anisotropy of crystals.¹ Crystal growth is a surface-controlled process in which reactant ions in solvent are incorporated into surface lattice sites to yield the bulk long-range order that determines crystalline materials.² Crystal shape control of noble metal nanocrystals^{3,4} as well as their alloys^{5–7} has received much attention due to their excellent shape-dependent performance in various catalytic reactions,⁸ surface plasmon resonance and surface enhanced Raman spectrum (SERS),⁹ etc. Noble metal nanocrystals are easy to grow with high index facets because these materials are composed of the same atoms, and the chemical bonds are metallic bonds with no orientation and saturation. Shape- and facet-dependent properties of many functional transitional metal oxide materials have also been reported, such as TiO₂,^{10,11} Cu₂O,^{12,13} and Fe₃O₄.^{14–16} Yang et al. reported that TiO₂ single crystals could be grown with a curved surface (facet with continuous Miller index) by just using citric acid and hydrofluoric acid as synergistic tailoring

agents.¹⁷ For more complex structure oxides, however, crystal shape and facet tailoring seems more challenging due to the complexity bonding relations between different kinds of atoms. Only a few representative oxides have been reported with a tailored crystal facet. Li et al. prepared BiVO₄ crystals with a different ratio of {010} and {110} facets, which shows facet-dependent activity for water oxidation under visible light irradiation.¹⁸ Ye et al. reported Ag₃PO₄ growth with rhombic dodecahedrons ({110} facets) and cubes ({100} facets), which exhibited facet-dependent activities in photocatalytic degradation of organic contaminants.¹⁹

Perovskite structure oxides are the most prominent mixed-oxide materials in heterogeneous catalysis due to the high catalytic activity and thermal stability.²⁰ However, the utilization of perovskite oxides is still limited, which may be because the most stable surface is usually terminated with

Received: August 16, 2016

Revised: September 20, 2016

Published: September 29, 2016

noncatalytically active crystal facets.^{21,22} High-index facets tailoring may be an effective route to improve the activity of perovskite structure catalysts. Until now, only several perovskite oxides have been reported on the crystal facet tailoring with well-defined polyhedral shapes.²³ AgNbO₃²⁴ and NaTaO₃²⁵ sub-micrometer single crystals with the shape of either cubes or polyhedrons could be prepared in hydrothermal conditions using ethylene glycol (EG) as a surfactant facet tailoring agent. Crystal shapes of SrTiO₃,²⁶ BaTiO₃,^{27,28} and BaZrO₃²⁹ could also be tailored by adding ethanol or a surfactant capping agent (e.g., polyethylene glycol, oleic acid) in the solutions of reactant chemicals. These reported perovskite structure oxides are mainly A^IB^VO₃ and A^{II}B^{IV}O₃ families. For the A^{III}B^{III}O₃ family, either primitive³⁰ or doped ABO₃,³¹ it seems that very few materials have been reported about their crystal facet and shape tailoring technique.

For perovskite structure ferrites, the synthesis of single-crystalline BiFeO₃ nanowire was reported via the hydrothermal method with only NaOH mineralizer in reactant solutions,³² while BiFeO₃ microplates with dominant (012) facets have also been reported.³³ Under the assistance of polyethylene glycol in hydrothermal condition, the shapes of BiFeO₃ single crystal could be tailored as a pill, rod, and cube under different concentrations of KOH.³⁴ Perovskite structure rare-earth orthoferrites (REFeO₃) are a main family semiconductor materials and show potential applications in catalysis,³⁵ gas sensors,³⁶ ferromagnetic and ferroelectric storage,³⁷ and so on. However, no report has been concentrated on the crystal facet and shape tailoring of REFeO₃. Although many methods have been applied to prepare REFeO₃ perovskite phase samples, such as sol-gel,³⁸ coprecipitation,³⁹ and traditional ceramic methods, most of these methods only result in polycrystals and crystals unable to grow with tailored facets. Recently, a direct low-temperature hydrothermal method has been used to produce high crystallinity and purity YFeO₃ microcrystals,⁴⁰ but the shapes are irregular without tailored facets. High quality REFeO₃ single crystal with a well controlled crystal plane surface could only be obtained from tediously cutting and polishing with a floating zone method.⁴¹ Thus, preparation and tailoring perovskite structure REFeO₃ single crystal shapes are important for further investigation of their surface structure and shape-dependent chemical reactions.

In our previous work, urea has been recognized as an efficient shape tailoring agent for controlled crystal facet growth in several perovskite structure compounds.⁴² Various shapes of La_{1-x}Sr_xMnO₃ crystals could be controllably prepared accordingly.⁴³ In this paper, we report a general method for tailoring the crystal shape on perovskite structure rare-earth ferrites (REFeO₃, RE = La, Pr, Sm, Dy, Er, Y) crystals in hydrothermal conditions. By adjusting the dosage of KOH and urea, cubic LaFeO₃ formed truncated cubes, PrFeO₃ perpendicular cross prisms, SmFeO₃ crossed bars with trustum, DyFeO₃ church tower-like blocks, ErFeO₃ distorted octahedrons, and YFeO₃ long bars and thick hexagonal elongated plates. Detailed shape tailoring conditions for each phase crystals have been discussed clearly. The structure of each REFeO₃ determines the shapes of single crystals that could be obtained and generally considered in other lanthanide REFeO₃ by discussion of the variance of reduced unit cell parameters in reference to ideal cubic ABO₃ perovskite structure. DyFeO₃ was taken as an example to discuss the crystal facet tailoring and growth mechanism based on the Bravais–Friedel–Donnay–Harker (BFDH) law. Shape-dependent magnetization of YFeO₃ is discussed finally. This

paper not only builds a general crystal shape tailoring technique for various shapes of REFeO₃ crystals, but also provides many crystals for further study and application of anisotropy either in physical or in chemical properties.

EXPERIMENTAL SECTION

Materials and Methods. Chemicals of La(NO₃)₃·6H₂O (99.9%), Pr(NO₃)₃·6H₂O (99.9%), Sm(NO₃)₃·6H₂O (99.9%), Dy(NO₃)₃·6H₂O (99.9%), Er(NO₃)₃·6H₂O (99.9%), Y(NO₃)₃·6H₂O (99.9%), Fe(NO₃)₃ (99.9%), CO(NH₂)₂ (99.99%), and analytical grade of KOH were purchased from Sinopharm Chemical Reagent Co. Ltd. All of the chemicals were used as received without any further purification. Solutions of 0.4 M RE(NO₃)₃ and Fe(NO₃)₃ were prepared with deionized water in advance. A crystal facet tailoring method and experimental procedure were adapted from our previous work.⁴² In detail, 5 mL solutions of RE(NO₃)₃ and Fe(NO₃)₃ were injected into a 50 mL glass beaker with continuous magnetic stirring for 10 min. Then different grams of KOH (Table 1) solid was added into the

Table 1. Sample Preparation Conditions of Various Shapes of REFeO₃ Microcrystals

sample	KOH	urea	shape
LaFeO ₃	4.5 g	1.5 g	cube
	5.0 g		truncated cube
	5.5 g		truncated elongated cube
PrFeO ₃	5.0 g	1.2 g	cube
		1.5 g	truncated cube
		1.8 g	iso-truncated cube
		2.0 g	perpendicular cross bar
SmFeO ₃	5.0 g	2.0 g	long bars with chamfer angles
	10.0 g	1.5 g	elongated cube
DyFeO ₃	5.0 g	2.0 g	elongated pyramid on cuboid
	6.0 g		trustum on cuboid
	7.0–8.0 g		truncated polyhedron
	9.0–10.0 g		truncated thick plate
ErFeO ₃	5.0 g	2.0 g	pyramid on cuboid
	6.0–7.0 g		truncated polyhedron
	8.0–10.0 g		truncated thick plate
YFeO ₃	5.0 g	2.0 g	elongated bar
	6.0 g		tailored bar
	7.0 g		tailored polyhedron

beaker and dissolved gradually in the reactant solution. The yellow solutions changed into a red slurry as soon as the KOH dissolved. After the whole mixture was cooled down to room temperature, different amounts of urea (CO(NH₂)₂) were added to the slurry and the mixture was stirred continuously for another 5 min. The overall controlled parameters are listed in Table 1. Then, the whole mixture was transferred into a 20 mL Teflon autoclave with a filling capacity ca. 75% and then kept at 240 °C for 48 h for all the REFeO₃ samples. After the synthesis reaction, the final dark red bright samples were obtained and subsequently washed with deionized water several times, and then dried at 70 °C for 2 h. The final products were crystalline and sealed into plastic sample tubes without post treatment.

Characterization and Physical Properties. Elemental composition of the products was analyzed by inductively coupled plasma atomic emission spectroscopy (ICP-AES), and the results are confirmed quite well with characterized X-ray energy dispersive spectroscopy (EDS). Powder X-ray diffraction (XRD) data were collected on a Rigaku D/Max 2500 V/PC X-ray diffractometer with CuK α radiation ($\lambda = 1.5418 \text{ \AA}$) at 50 kV and 200 mA with a scan speed of 5°/min at room temperature in the angle range of $10^\circ \leq 2\theta \leq 80^\circ$ with an increment of 0.02°. Scanning electron microscope (SEM) images were collected with a Helios NanoLab 600i Dual Beam System, FEI Company, America. Electron backscattered diffraction (EBSD) characterization for single crystals was performed on Magellan XHR

400L FE-SEM (FEI Company, U.S.A.), equipped with NordlysNano EBSD detector and corresponding pattern analyzing software (Oxford Instrument, U.K.). The Kikuchi patterns are generated at an acceleration voltage of 30 kV and a beam current of 2.5 nA, recorded by means of a low-light CCD camera. The resulting patterns were further analyzed and indexed using the analysis software package. Direct current (DC) hysteresis loops, zero-field-cooled (ZFC), and field-cooled (FC) magnetization measurements were performed on a superconducting quantum interference device (SQUID) magnetometer (Quantum Design) from 4 to 380 K.

RESULTS AND DISCUSSION

Shape Evolution of LaFeO₃ Crystals. The primitive shape of hydrothermally grown LaFeO₃ crystals is nearly cubes with a little longer length of one axis.⁴⁴ Phase purity of the as-prepared LaFeO₃ by modified hydrothermal method was examined by powder XRD in Figure S1. Crystal shape tailoring process is performed by tailoring the concentration of KOH and urea in hydrothermal conditions similar to LaFeO₃ synthesis. When 1.5 g of urea was added in the reactant solution, the cubes form truncated cubes along the 12 edges of each cube. This may be due to the capping effect of NH₄⁺ that is from the decomposition of urea at elevated temperature in hydrothermal autoclaves. Cubes are obtained when not enough KOH (4.5 g) is added in the system (Figure 1a,b), and when more KOH (5.0 g) was used, the cube crystals are truncated (Figure 1c,d). This result indicates that the crystal shapes of LaFeO₃ crystals are dependent on the concentration of K⁺ in the crystal growth process in the presence of NH₄⁺. Particle size distribution of each shape of LaFeO₃ crystals is shown in Figure S2. The size

distribution and average (ca. 20 μm) are nearly the same in all the particles grown with different shapes.

In the hydrothermal method preparation of perovskite structure LaFeO₃, no samples could be synthesized if only KOH was added in the reactive system as a mineralizer. When a carbonate precursor (i.e., chemicals contain CO₃²⁻) was put into the autoclave, a LaFeO₃ pure phase sample could be prepared.⁴⁴ For the synthesis of other perovskite structure rare-earth ferrites, pure phase samples could be prepared when KOH was used as the sole mineralizer.⁴⁵ This may be because the size of La³⁺ is much larger than that of other rare-earth cations. In hydrothermal crystallization processes of perovskite structure oxides, precursors of mixed hydroxides were formed in advance.⁴⁶ These transition metal or rare-earth hydroxides usually formed layered structures with anions inserted between the layers of metal hydroxide.⁴⁷ When the reaction temperature increases, the pressure inside of the autoclave gets higher. This effect makes the near neighbor hydroxide groups polymerize by forming M–O–M linkages. In crystallization processes, rare-earth cations transport into the interlayers of ferrite hydroxides and release H₂O molecules to form the basic perovskite structure connections. For other rare-earth cations, the sizes are much smaller than that of La³⁺, which makes them easy to migrate into the layers of ferrite hydroxides. Thus, in these perovskite compound preparation processes, no larger anion groups are needed to expand the interlayer space of ferrite hydroxides. For LaFeO₃, however, La³⁺ is much larger than the others. If the layers of ferrite hydroxides are mainly NO₃⁻ insertion, the layer distances are not large enough for La³⁺ transportation. Thus, when carbonates are introduced to the reaction media, LaFeO₃ could be prepared.

Shape Evolution of PrFeO₃ Crystals. PrFeO₃ crystallizes in a similar structure as that of LaFeO₃. However, the size of Pr³⁺ is smaller than that of La³⁺. This makes more distortion of the corner-sharing neighbor FeO₆ octahedron in the crystal lattice, although the full crystallization processes in pure KOH media make the final shape of PrFeO₃ a rectangular morphology.⁴⁵ When a small amount of urea (Figure 2a) was added into the reactant mixture, the PrFeO₃ crystal grows into cubes. By introducing more content of urea (1.5 and 1.8 g in Figure 2b,c), the shape evolution of this compound is similar as in the LaFeO₃ shape tailoring process. Perpendicular cross bar shape crystals of PrFeO₃ were obtained when the content of urea is 2.0 g with other conditions unchanged (Figure 2d). A similar phenomenon has never occurred in LaFeO₃ by changing the amount of KOH or urea. This difference may result from the effect of competition between K⁺ and NH₄⁺ on crystal building block stacking during the crystal growth process.

Shape Evolution of SmFeO₃ Crystals. Phase purity of the as-prepared SmFeO₃ by the modified hydrothermal method was examined by powder XRD in Figure S3. The shape of SmFeO₃ crystals could be tailored by variation of the KOH/urea ratio greatly. When the KOH/urea ratio = 5.0 g/2.0 g, crossed rectangular bars with small trustum of pyramid can be grown (Figure 3a,b). This synthesis condition is the same as that of PrFeO₃ in Figure 2d. But the bars are not perpendicular to each other. Although the crystal space group of SmFeO₃ is also *Pbnm*, the same as that of PrFeO₃, the distortion of FeO₆ octahedron is very severe.^{45,48} However, when the KOH/urea ratio = 10.0 g/1.5 g, the crystals grow into a large cuboid (Figure 3c,d). In this condition, K⁺ plays the dominant role in crystal growth, while NH₄⁺ cations are more prone to get into the gaseous form as NH₃ due to a higher concentration of OH⁻

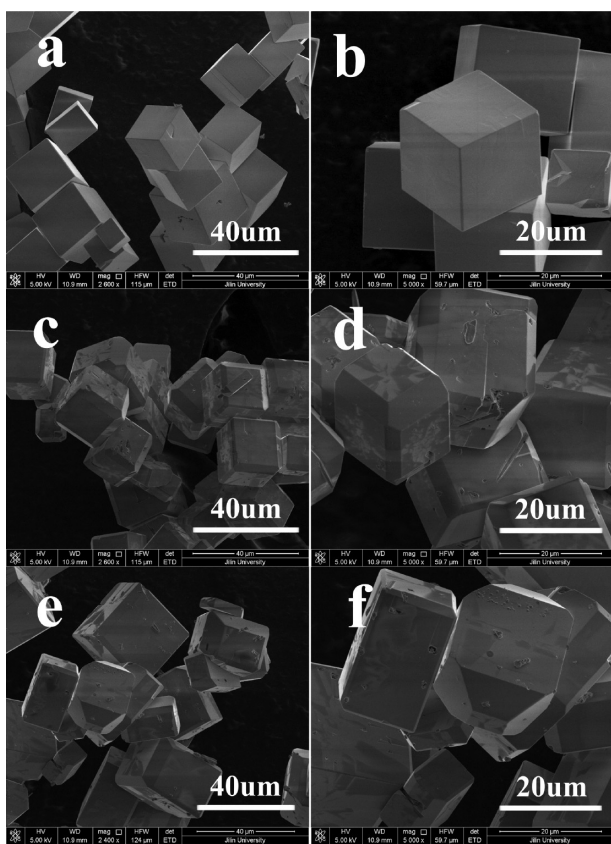


Figure 1. SEM graphs of the effect of KOH concentration on LaFeO₃ shape growth: 4.5 g (a, b), 5.0 g (c, d), 5.5 g (e, f).

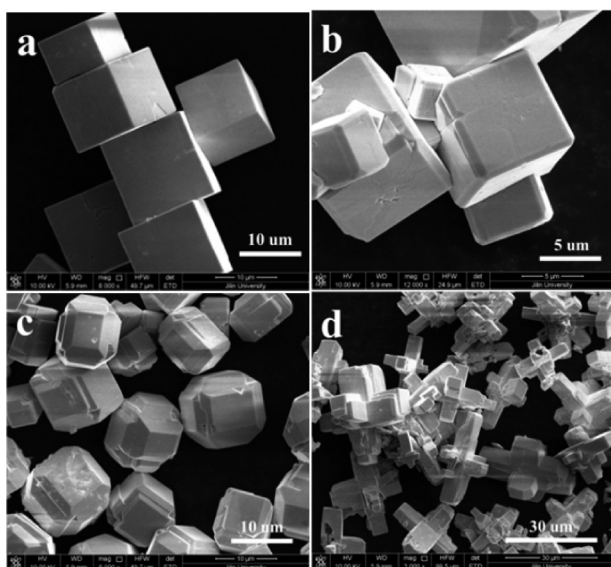


Figure 2. PrFeO₃ crystal growth under different urea contents: (a) cubes with KOH/urea = 5.0 g/1.2 g, (b) truncated cubes with KOH/urea = 5.0 g/1.5 g, (c) polyhedrons with KOH/urea = 5.0 g/1.8 g, and (d) perpendicular cross bars with KOH/urea = 5.0 g/2.0 g.

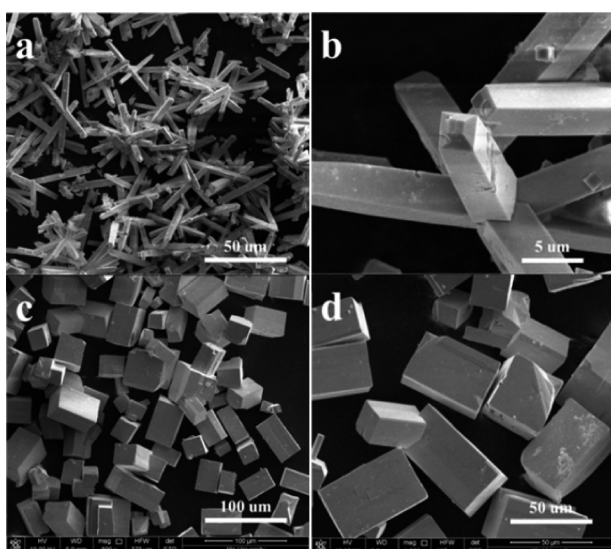


Figure 3. Low and high magnification SEM graphs of SmFeO₃: (a, b) rectangular rods with KOH/urea ratio = 5.0 g/2.0 g, (c, d) elongated cubes with KOH/urea ratio = 10.0 g/1.5 g.

in the reactant mixture following the reaction of $\text{NH}_4^+ + \text{OH}^- \leftrightarrow \text{NH}_3 + \text{H}_2\text{O}$. The concentration of NH_4^+ is less and K^+ is more compared that in Figure 3a,b, which makes the crystal grow more slowly in the {100} direction rather than {111} due to the lost capping effect of NH_4^+ toward FeO₆ octahedral groups, and the final crystal shape is elongated cubes. This result is similar to that of NdFeO₃ prepared in different concentrations of KOH with the hydrothermal method.⁴⁹

Shape Evolution of DyFeO₃ Crystals. Phase purity of the as-prepared DyFeO₃ by a modified hydrothermal method was examined by powder XRD in Figure S4. Crystals of hydrothermally synthesized DyFeO₃ are shown in Figure 4. When the concentration of KOH and urea is 5.0 and 2.0 g in a 10 mL reactant mixture, church tower-shape DyFeO₃ single crystals could be prepared. By keeping urea concentration

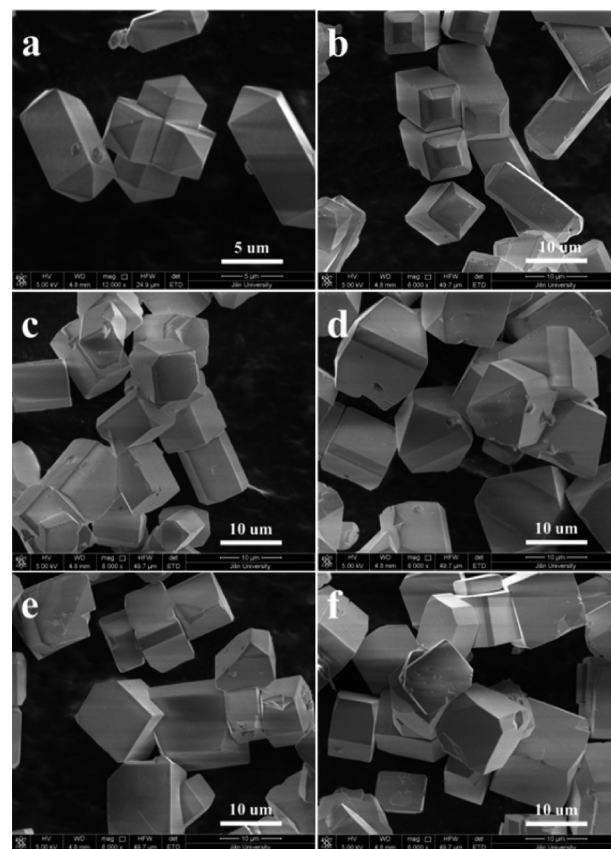


Figure 4. SEM graphs of DyFeO₃ crystals with different shapes: the ratio of KOH/urea are (a) 5.0 g/2.0 g, (b) 6.0 g/2.0 g, (c) 7.0 g/2.0 g, (d) 8.0 g/2.0 g, (e) 9.0 g/2.0 g, (f) 10.0 g/2.0 g, respectively.

constant while increasing the KOH content, the shape of DyFeO₃ can evolve from elongated pyramid on cuboid (Figure 4a) to the final polyhedral-shape crystals (Figure 4f). The tips of the pyramid changed into a trustum of a pyramid when 20% more of KOH was added in the reactive solution (Figure 4b). When 40% more KOH (i.e., 7.0 g) was dissolved in the reaction processes, the trustum disappeared and a feldspar-shape stubby DyFeO₃ crystal was shown (Figure 4c). When 60% or more KOH was added in the mixed solvents, the final shape of DyFeO₃ changed into truncated polyhedral shapes at last (Figure 4d). DyFeO₃ single crystals prepared with the hydrothermal method without any surfactant addition show a tabular shape when the concentration of KOH is ca. 4–9 M.⁴⁵ In comparison with the cuboid shape in a large cation size of La³⁺ and Pr³⁺, the occurring tabular shape of DyFeO₃ and ErFeO₃ is because the divergence of unit cell axis length gets bigger from LaFeO₃ to the smaller sized Dy³⁺ and Er³⁺ occupied A-site REFeO₃. When NH₄⁺ is introduced into the reactive conditions, it blocks the crystal growth along the face of FeO₆ octahedron direction. Thus, the shape of DyFeO₃ crystals was tailored in different concentrations of NH₄⁺ while keeping other conditions constant. Particle size distribution graphs for all the shape of DyFeO₃ samples are shown in Figure S5. The size is measured by the longest side of each crystal in SEM graphs. When 6.0 g of KOH and 2.0 g of urea were added in the reactant solution, the crystals can grow into the longest trustum ended rectangular blocks (ca. 20 μm).

Shape Evolution of ErFeO₃ Crystals. Phase purity of the as-prepared ErFeO₃ by modified hydrothermal method was

examined by powder XRD in Figure S6. Crystal shape evolution of ErFeO_3 in different concentration of urea is similar as that of DyFeO_3 . The tower-like pyramid on the cube shape of ErFeO_3 is not as long as that of the DyFeO_3 cuboid (Figure 5a), and between the rectangular facets, the crystal

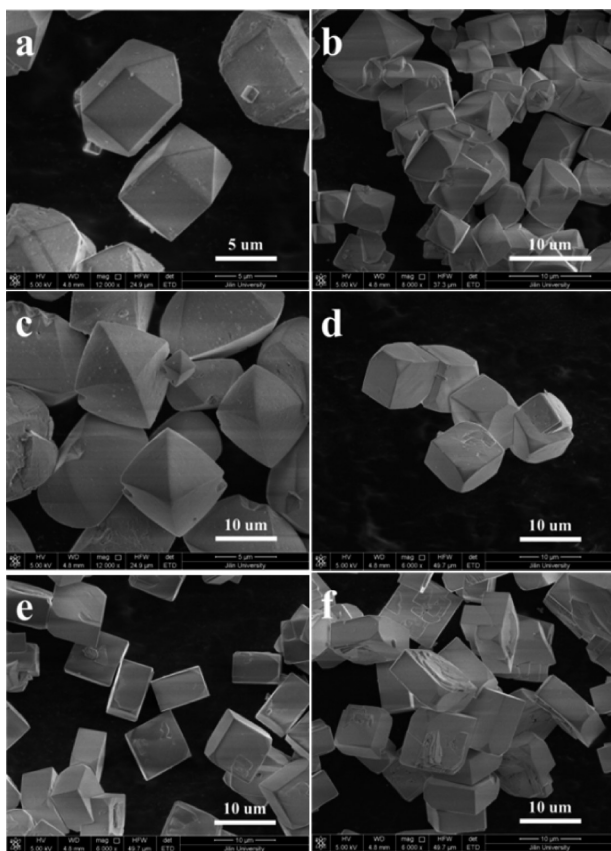


Figure 5. SEM graphs of ErFeO_3 crystals with different shapes: the ratio of KOH/urea is (a) 5.0 g/2.0 g, (b) 6.0 g/2.0 g, (c) 7.0 g/2.0 g, (d) 8.0 g/2.0 g, (e) 9.0 g/2.0 g, and (f) 10.0 g/2.0 g, respectively.

exposes an elongated hexagonal facet. Some facets get lost when 20% more KOH was added in reaction conditions (Figure 5b). When the content of KOH is 7.0 g, while keeping urea at 2.0 g, distorted polyhedron shape crystals were obtained (Figure 5c). By further increasing KOH in the reactant solutions, rhombus thick plate crystals were obtained (Figure 5e,f), which is similar to that of the no urea added traditional hydrothermal method.⁴⁵ Particle size distribution of ErFeO_3 crystals is shown in Figure S7. Pyramids on rectangular block shape ErFeO_3 show the longest with the length of ca. 10.5 μm . The particle sizes for all of ErFeO_3 are almost on the same size scale, which means that the addition of urea is not a critical factor in the size of ErFeO_3 in hydrothermal conditions.

Shape Evolution of YFeO_3 Crystals. Phase purity of the as-prepared YFeO_3 by a modified hydrothermal method was examined by powder XRD in Figure S8. Low and high magnification SEM graphs of shape controlled growth of YFeO_3 microcrystals prepared in different KOH concentration are shown in Figure 6. Powder XRD patterns for as-prepared YFeO_3 microcrystals are shown in Figure S8. They are all crystallized into the orthorhombic structure of the $Pnma$ space group, and the JCPDS card No. is 39-1489. When the amount of mineralizer is 5.0 g, the YFeO_3 crystal forms prisms with two

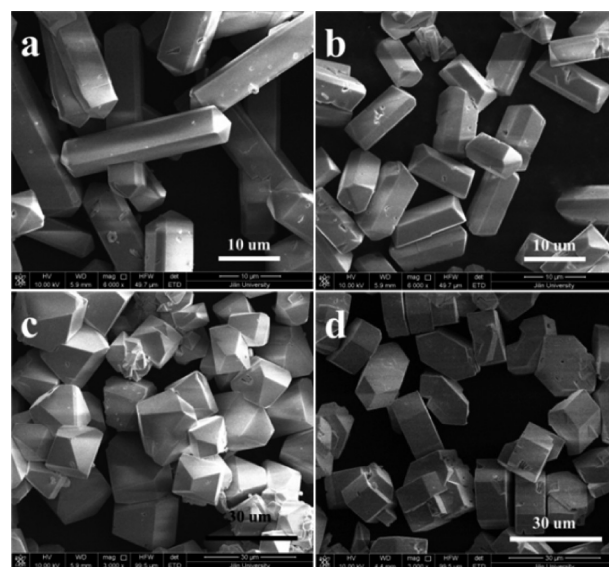


Figure 6. YFeO_3 hydrothermal growth with different KOH/urea ratios: (a) 5.0 g/2.0 g, (b) 6.0 g/2.0 g, (c) 7.0 g/2.0 g, and (d) 5.0 g/1.5 g, respectively.

pyramids further grown outside of the two end surfaces of prisms (Figure 6a), which is similar to that of DyFeO_3 and ErFeO_3 under the same synthesis condition. The prisms are ca. 30 μm in length and 7 μm in width and height, respectively. And the final shape is enclosed by four rectangles, eight triangles, and two elongated hexagons. The two pyramids grow on each side of the rod shape of YFeO_3 , which is due to the interaction of the FeO_6 octahedral group and NH_4^+ in this synthesis condition.

When KOH concentration is 6.0 g, the length of prism gets shorter, and the shapes change into two truncated triangle prisms on a rectangular slab (Figure 6b). That means more KOH can reduce the b -axis growth speed. Similar results also been reported in hydrothermally prepared NdFeO_3 ⁴⁹ and LuFeO_3 ⁵⁰ crystals. However, in a barely KOH environment, only the bar length could be modulated; the shapes, i.e., the enclosed facet of crystal, are not changed. When the KOH amount is 7.0 g, feldspar-shape stubby YFeO_3 crystals were obtained (Figure 6c). Hexagonal thick plate shape samples were prepared when the mineralizer and urea content was lowered to 5.0 and 1.5 g, respectively. This result indicates that NH_4^+ has played an important role in the shape and facet modulation in the YFeO_3 single crystal growth process. Particle size distribution of YFeO_3 crystals is shown in Figure S9. The average length of YFeO_3 -rod is ca. 28 μm , while the length of the short YFeO_3 rod (Figure 6b) is ca. 10.5 μm . Feldspar and hexagonal thick plate shape YFeO_3 crystals are both nearly 22 μm on average. The shape difference in YFeO_3 is the most evident than other REFeO_3 in this paper, which means it is the most suitable compound to study the shape-dependent physical properties. Besides, the f - and d -orbitals of Y^{3+} are unoccupied with any electrons, which means no A-site spin contribution to the magnetism in YFeO_3 .

The electron backscattered diffraction (EBSD) method is a powerful technique to characterize crystalline particle orientation with different shapes and morphology. Kikuchi patterns of oriented YFeO_3 single crystal enclosed by different facets are given in Figure S10. The diffraction result of definite crystal facet should be collected with a tilt angle of the stage for

information collection. Thus, the SEM image of YFeO_3 is elongated horizontally (Figure S10a). The Kikuchi pattern of the YFeO_3 crystal was collected at the bright surface in SEM image, and the resulting pattern is shown in Figure S10b and indexed in (c). Many Kikuchi bands intersect at the (101) zone, which means the secondary electrons are mainly distracted by (101) facet on the bright surface of the selected YFeO_3 crystal in the SEM image. Thus, the exposed facet should be the (101) facet of YFeO_3 .

Shape Evolution Mechanism of REFeO_3 . From previous results of the crystal facet and shape tailoring process of the series of rare-earth ferrites REFeO_3 , we found that the ratio of mineralizer to urea concentration plays an important role in the REFeO_3 hydrothermal crystallization system.⁴² Without urea or NH_4^+ species adding to the reactants, the shapes are nearly impossible to tailor by only changing the concentration of KOH. At high concentration of KOH, it may affect the growing rate along the $\langle 010 \rangle$ and $\langle 101 \rangle$ directions. More KOH in the reactant solution seems to accelerate the growing speed along the $\langle 010 \rangle$ direction according to Xing's work.⁴⁹ The tailoring effect, however, is very limited in the only KOH environment. In our previous work, we found the crystal facet tailoring effect of NH_4^+ (decomposed from urea) in several Cr-, Mn-, and Fe-based perovskite structure oxides^{42,43} and indicated that NH_4^+ should be a special tailoring agent for perovskite structure facets due to its small size, positive charge, and tetrahedral symmetrical structure. The interaction between NH_4^+ and BO_6 octahedral groups may follow two ways: eclipsed conformation and staggered conformation (Figure 7). Either of them is stable

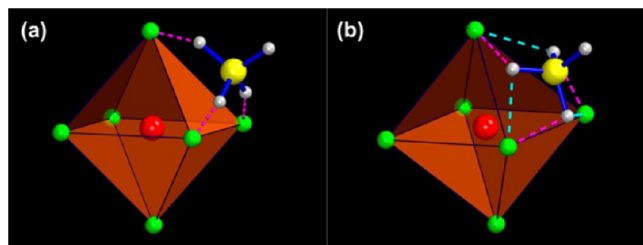


Figure 7. Two possible coordinate ways of NH_4^+ to BO_6 octahedron: (a) eclipsed conformation and (b) staggered conformation. B-site atom: red ball; O: green ball; N: yellow ball; H: gray ball.

in regular octahedron shape of BO_6 groups. For most of perovskite structure oxides, the BO_6 octahedron is distorted due to the A-site cation size mismatch and the resulted divergence of tolerance factor from 1 in the ideal $Pm\bar{3}m$ perovskite. For perovskite oxides with distorted octahedron, staggered conformation will be more stable. In this conformation, NH_4^+ could change its orientation to meet the coordination with oxygen on BO_6 octahedron by varying the bond length of hydrogen bonds as indicated by dashed lines in Figure 7. The capping and blocking effect of NH_4^+ and the competition with K^+ in hydrothermal synthesis of perovskite structure oxides have been discussed in shape tailoring process of $\text{La}_{1-x}\text{Sr}_x\text{MnO}_3$ crystals.⁴³ Staggered conformation makes it easier to tailor any family of perovskite oxides theoretically by changing its coordinate orientation of NH_4^+ .

From previous discussions on the shape evolution phenomena of different A-site rare-earth cations occupied perovskite structure ferrites, we found an interesting change in the corresponding shape evolution process due to A-site cation sizes and crystal structure of REFeO_3 . Thus, we summarized

the reduced unit cell parameters of different A-site rare-earth ferrites in Table S2. The primitive reduced unit cell parameters are calculated based on the following formula: $a_p = a/\sqrt{2}$, $b_p = b/\sqrt{2}$, $c_p = c/2$ (for $Pbnm$ space group) or $a_p = a/\sqrt{2}$, $b_p = b/2$, $c_p = c/\sqrt{2}$ (for $Pnma$ space group). From Table S1, it can be seen that with the increasing atomic number of rare-earth elements, i.e., decreasing the size of A-site atoms, the difference of the length of reduced unit cell parameters is changed gradually. To clearly show this effect, variance of the length of a_p , b_p , c_p for each REFeO_3 was calculated based on the equation of variance formula: s^2 (variance) = $\frac{(a_p - e)^2 + (b_p - e)^2 + (c_p - e)^2}{3}$, in which e (expectation) = $\frac{a_p + b_p + c_p}{3}$. The variance for the axis length of each REFeO_3 gets larger when the atomic number is increased (Figure 8). For the REFeO_3 with small variance, the

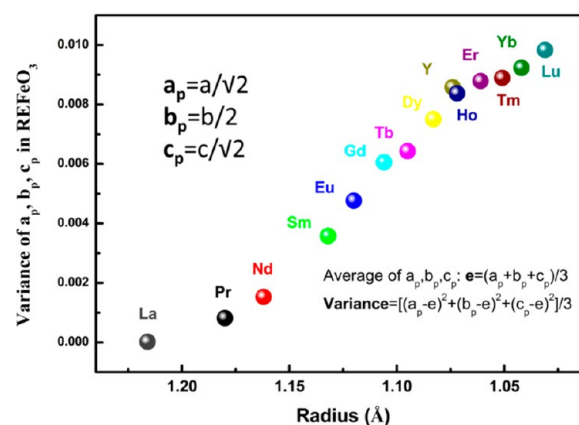


Figure 8. Variance of a_p , b_p , c_p in REFeO_3 compounds. The variance for each REFeO_3 is calculated by the equation: s^2 (variance) = $[(a_p - e)^2 + (b_p - e)^2 + (c_p - e)^2]/3$, in which e (expectation) = $(a_p + b_p + c_p)/3$.

crystal shape is more prone to grow as cubic; in contrast, the crystals with a large variance are prone to grow in elongated rods or thin plates. Variance of reduced unit cell parameters in REFeO_3 indicates the degree of distortion of the FeO_6 octahedron. Crystal facet tailoring in REFeO_3 with NH_4^+ is mainly dependent on the capping effect on the FeO_6 octahedron, which means the distortion of FeO_6 in the crystal structure defines the possibility of the final crystal shapes. Thus, crystal shape and facet tailoring of perovskite structure oxides should be based on the crystal structure characteristics.

The morphological variety of crystal habits is due to differences in relative growth rates of faces of which the crystal is composed. For equilibrium, the growth rates of faces are proportional to the distances from the center of the crystal to the respective hkl faces. According to the BFDH law, such distances are inversely proportional to the interplanar distances; therefore, the observed crystal faces are those with the largest interplanar distances. The shape and facet evolution process of DyFeO_3 crystals in NH_4^+ mediated hydrothermal conditions was taken as an example to show the relationship of crystal growth in different facets based on the BFDH theory (Figure 9). According to the theoretical shape of DyFeO_3 crystal calculated by the $Pbnm$ structure, this crystal will be exposed $\{110\}$, $\{002\}$, $\{101\}$, $\{020\}$, $\{111\}$, and $\{021\}$ facets if it grows freely without any facet capping and shape tailoring agents (Figure 9f). According to the XRD pattern of DyFeO_3 (Figure

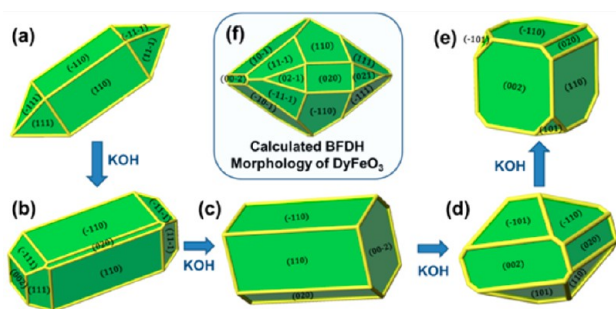


Figure 9. (a–e) Crystal shape changes with different indexed crystal facet evolution of DyFeO_3 in NH_4^+ and KOH hydrothermal condition and (f) Calculated morphology of DyFeO_3 based on THE BFDH method.

S4), $\{101\}$ facets show the largest interplanar distance among these facets. Theoretically, this family of facets should be kept as the exposed facets at the final crystal surface. However, $\{101\}$ facets show more faces of BO_6 octahedrons (Figure 10),

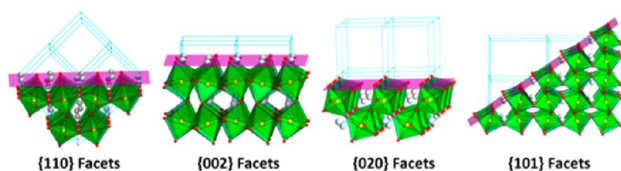


Figure 10. Crystal structure of different facets in DyFeO_3 .

which is unfavorable in solely OH^- media. Thus, in solely KOH mineralizer reactive conditions, DyFeO_3 crystals grow into a cuboids-like shape,⁴⁵ which may be enclosed by four of $\{110\}$ and two of $\{002\}$ facets. As shown in Figure 10, $\{110\}$ and $\{002\}$ facets of DyFeO_3 are mainly terminated with the Dy–O layer. Surface Dy^{3+} could be stabilized by OH^- due to the high concentration of KOH in reactive solutions. With a definite concentration of KOH/urea, crystals with four rectangular $\{110\}$ facets and eight triangle $\{111\}$ facets are grown (Figure 9a). By increasing the content of KOH, the area of $\{111\}$ facets are reduced, and $\{002\}$ and $\{020\}$ facets are exposed (Figure 9b). These results indicate that although $\{110\}$ and $\{002\}$ facets are both KOH favorable, $\{110\}$ facets show more uniform distribution of Dy–O bonds, which means they are more stable than $\{002\}$ facets. For $\{020\}$ facets, however, they are mainly terminated by BO_6 octahedron faces, which is only stable in NH_4^+ content media. $\{111\}$ facets are not very stable to expose a clear plane of surfaces; in these crystals (Figure 9a,b), it may be composed by steps of $\{110\}$ and $\{002\}$ facets, but this inference needs further evidence. Further increasing the KOH content, $\{111\}$ facets get lost and the area of $\{110\}$ and $\{002\}$ facets get enlarged (Figure 9c). $\{101\}$ facets will be exposed at the point of the KOH concentration being nearly doubled (Figure 9d,e). More of KOH still decreases the area of $\{101\}$ facets. Thus, we may draw a conclusion that $\{111\}$ facets are mainly NH_4^+ stabilized, $\{110\}$ and $\{002\}$ facets are OH^- stabilized, $\{020\}$ and $\{101\}$ facets are both NH_4^+ and OH^- costabilized.

Figure 10 shows THE crystal facet structure of DyFeO_3 in each exposed facets for different shapes of crystals. $\{110\}$ facets are the most stable facets, which are terminated with the Dy–O layer with a uniformly distributed Dy–O bond in each direction in-plane. The unsaturated chemical bond of the surface Dy can be balanced by OH^- in reactive solution due to the strong

alkaline (KOH) addition. $\{002\}$ facets show a similar d -value and surface composition as that of $\{110\}$. However, the Dy–O distribution is not as uniform as that of $\{110\}$, which makes it less stable than $\{110\}$. $\{020\}$ and $\{101\}$ facets are mainly exposed to one of the faces of the FeO_6 octahedron at the surface, which are NH_4^+ stabilized facets. Thus, the facet habitat difference makes it possible to tailor the growing speed in each direction of crystals from seed and finally determine the shape of crystals.

Shape-Dependent Magnetic Properties of YFeO_3 .

Previously, size-dependent effect magnetic properties of materials have been found in many perovskite structure oxides, such as BaFeO_3 ⁵¹ and YbMnO_3 .⁵² YFeO_3 crystallizes in the D_{2h}^{16} $Pnma$ space group with a distorted perovskite structure,⁵³ which is a canted antiferromagnet ($T_N \approx 650$ K) because the atomic moments align at an angle to the c -axis. The weak ferromagnetism in YFeO_3 is mainly caused by anisotropic superexchange.⁵⁴ Anisotropic magnetic behavior has been reported in the floating zone method grown YFeO_3 single crystal, in which magnetization normal to the (100) direction shows the largest coercive field and parallel to (100) the biggest saturation magnetization.⁵⁵ In this article, we found shape-dependent magnetic properties in different YFeO_3 microscale crystals. Figure 11 shows the temperature- and field-dependent magnetic behavior for each shape of YFeO_3 microcrystal sample. All of three YFeO_3 samples show weak ferromagnetism from 4 to 380 K. Usually, due to the strong positively charged Fe^{3+} with a small ionic size, each Fe ion is a ligand with six O ions forming a FeO_6 octahedron, and the O is the bridge for adjacent two octahedrons, which may act as a media for superexchange interaction of d electrons in neighboring Fe^{3+} . As can be seen in Figure 11a, YFeO_3 –K1 crystals show a typical canted magnetization curve in ZFC–FC curves. With increasing temperature, magnetization is reduced gradually, and until 380 K, the residue magnetization is still 0.22 emu/g in the FC curve. In the hysteresis curve at 5 K, the saturated and remnant magnetization is much higher than that of 50 and 300 K, suggesting that Fe^{3+} spins are not perfectly antiparallel but slightly canted. By increasing the sample temperature, the residual magnetization decreases whereas the coercive field increases. The coercive field at room temperature is up to 8000, 10800, and 10600 Oe for rod-, feldspar-, and polyhedron-shape YFeO_3 crystals, respectively. The hysteresis loops for all YFeO_3 samples are not saturated up to 3 T field at 5, 50, and 300 K, respectively. Remnant magnetizations are approximately 0.85–1.0 emu/g at several temperature points.

In YFeO_3 , the G-type antiferromagnetic ordering is along the a -axis, the weak ferromagnetism is along the c -axis, and the weak antiferromagnetism is along b -axis.⁵⁶ As shown in Figure 12a, typical antiferromagnetic ordering is along the a -axis with antiparallel of Fe^{3+} spin with a small canted angle along the b -axis. In the c -axis direction, the canted angle for all Fe^{3+} spin is parallel arrangement, which indicates weak magnetism (Figure 12b). YFeO_3 rods are grown along the b -axis, and thus when the crystalline samples are sealed in plastic tubes, they will form uniformly stacked powder pillars and expose more directions perpendicular to the b -axis, which makes more ferromagnetic ordering crystal directions along the magnetic field during magnetization measurement in VSM. Thus, the YFeO_3 rod sample shows higher magnetization in either FC–ZFC results or saturated and remnant magnetization at 4 K (Figure 11a). For the other two shapes of YFeO_3 crystals, no such obvious spin–lattice orientation was shown in both shapes of crystals.

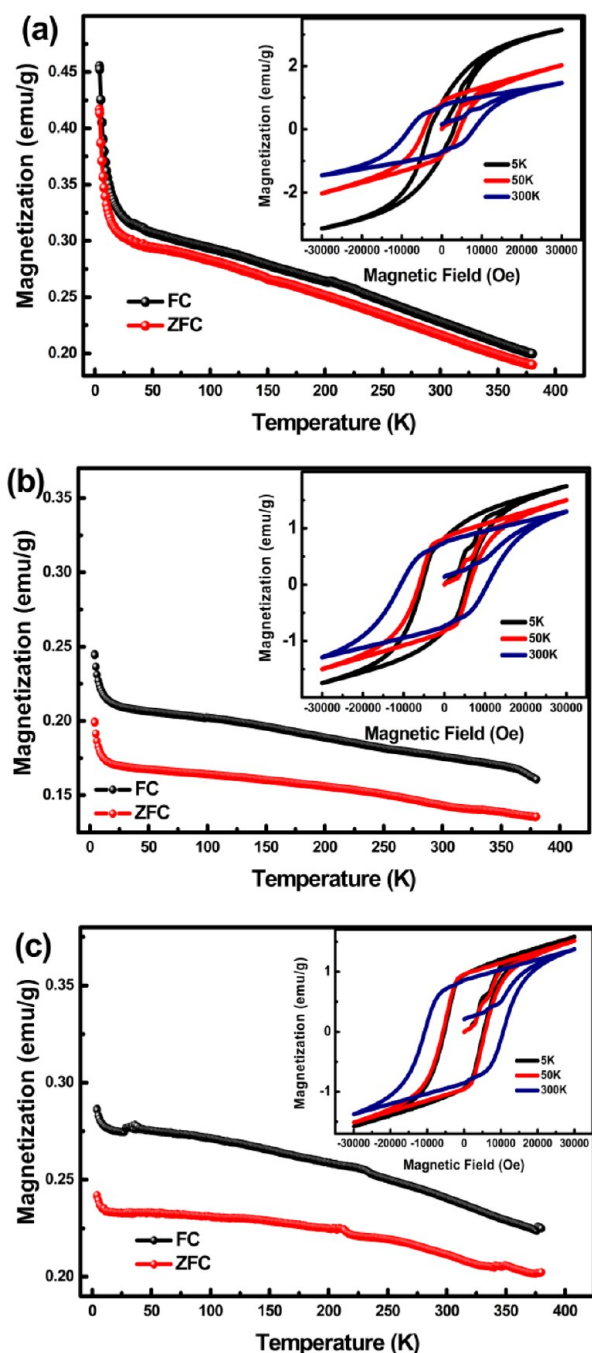


Figure 11. Magnetic behaviors for each shape of YFeO_3 microcrystals. (a–c) Direct current field cooling (FC) and zero-field cooling (ZFC) magnetization and hysteresis (inset) curves of YFeO_3 -rod, YFeO_3 -feldspar, and YFeO_3 -polyhedron, respectively.

CONCLUSIONS

In conclusion, we have developed an effective method to tailor the shape and facet growth of various REFeO_3 ($\text{RE} = \text{La}, \text{Pr}, \text{Sm}, \text{Dy}, \text{Er}, \text{Y}$) microcrystals in hydrothermal conditions. The crystal growth rate in each direction could be controlled by properly controlling the relative ratio of NH_4^+/KOH . By adjusting the dosage of KOH and urea, cubic LaFeO_3 formed truncated cubes, PrFeO_3 perpendicular cross prisms, SmFeO_3 crossed bars with trustum, DyFeO_3 church tower-like blocks, ErFeO_3 distorted octahedrons, and YFeO_3 long bars and thick hexagonal elongated plates. Crystal growth mechanism for each

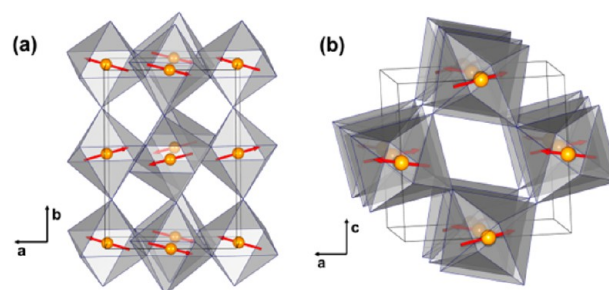


Figure 12. Magnetic structure of YFeO_3 : view from the (a) c - and (b) b -axis, respectively.

shape of REFeO_3 was discussed. Temperature- and magnetic field-dependent magnetization curves for YFeO_3 show shape divergence due to the anisotropy of crystals. Hysteresis loops analysis of bar-shaped YFeO_3 show the highest magnetization and lowest coercive field. These results indicate that (1) facet- and shape-controlled crystal growth should be based on the unit cell of the primary structure, and (2) powder magnetization characterization may be dependent on the shapes of crystals. This paper not only builds a general crystal shape tailoring technique for various shapes of REFeO_3 crystals, but also provides many crystals for further study and application of anisotropy either in physical or in chemical properties.

ASSOCIATED CONTENT

Supporting Information

The Supporting Information is available free of charge on the ACS Publications website at DOI: 10.1021/acs.cgd.6b01219.

Powder X-ray diffraction pattern of as-prepared REFeO_3 samples, particle size distribution graphs for each shape REFeO_3 crystals, EBSD Kikuchi patterns of YFeO_3 , table of reduced unit cell of REFeO_3 adapted from JCPDS Card (PDF)

AUTHOR INFORMATION

Corresponding Author

*E-mail: shfeng@jlu.edu.cn.

Notes

The authors declare no competing financial interest.

ACKNOWLEDGMENTS

This work was supported by the National Natural Science Foundation of China (Grants 21427802 and 21671076). The authors would like to acknowledge the Open Project Program of State Key Laboratory of Inorganic Synthesis and Preparative Chemistry, Jilin University, and the “Twelfth Five Year” Project of Science and Technology Research in the Education Department of Jilin Province (No. 2015-466) and Natural Science Fund of Jilin Provincial Science & Technology Department (No. 20160101326JC).

REFERENCES

- (1) Dhanaraj, G.; Byrappa, K.; Prasad, V.; Dudley, M. *Springer Handbook of Crystal Growth*; Springer-Verlag: Berlin, 2010.
- (2) Dandekar, P.; Kuvadia, Z. B.; Doherty, M. F. *Annu. Rev. Mater. Res.* **2013**, *43*, 359.
- (3) Xiong, Y.; Wiley, B. J.; Xia, Y. *Angew. Chem., Int. Ed.* **2007**, *46*, 7157.
- (4) Tao, A. R.; Habas, S.; Yang, P. *Small* **2008**, *4*, 310.

- (5) He, W.; Wu, X.; Liu, J.; Hu, X.; Zhang, K.; Hou, S.; Zhou, W.; Xie, S. *Chem. Mater.* **2010**, *22* (9), 2988.
- (6) Yuan, Q.; Wang, X. *Nanoscale* **2010**, *2*, 2328.
- (7) Jia, Y.; Cao, Z.; Chen, Q.; Jiang, Y.; Xie, Z.; Zheng, L. *Sci. Bull.* **2015**, *60*, 1002.
- (8) Zhou, K.; Li, Y. *Angew. Chem., Int. Ed.* **2012**, *51*, 602.
- (9) Li, Y.; Liu, Q.; Shen, W. *Dalton Trans.* **2011**, *40*, 5811.
- (10) Liu, G.; Yang, H. G.; Pan, J.; Yang, Y. Q.; Lu, G. Q.; Cheng, H.-M. *Chem. Rev.* **2014**, *114*, 9559.
- (11) Lu, Y.; Zang, Y.; Zhang, H.; Zhang, Y.; Wang, G.; Zhao, H. *Sci. Bull.* **2016**, *61*, 1003.
- (12) Kuo, C.-H.; Huang, M. H. *Nano Today* **2010**, *5*, 106.
- (13) Huang, M. H.; Rej, S.; Hsu, S.-C. *Chem. Commun.* **2014**, *50*, 1634.
- (14) Ho, C.-H.; Tsai, C.-P.; Chung, C.-C.; Tsai, C.-Y.; Chen, F.-R.; Lin, H.-J.; Lai, C.-H. *Chem. Mater.* **2011**, *23* (7), 1753.
- (15) Cheng, X.-L.; Jiang, J.-S.; Jiang, D.-M.; Zhao, Z.-J. *J. Phys. Chem. C* **2014**, *118* (24), 12588.
- (16) Zhou, Z.; Zhu, X.; Wu, D.; Chen, Q.; Huang, D.; Sun, C.; Xin, J.; Ni, K.; Gao, S. *Chem. Mater.* **2015**, *27*, 3505.
- (17) Yang, S.; Yang, B. X.; Wu, L.; Li, Y. H.; Liu, P.; Zhao, H.; Yu, Y. Y.; Gong, X. Q.; Yang, H. G. *Nat. Commun.* **2014**, *5*, 5355.
- (18) Wang, D.; Jiang, H.; Zong, X.; Xu, Q.; Ma, Y.; Li, G.; Li, C. *Chem. - Eur. J.* **2011**, *17* (4), 1275.
- (19) Bi, Y.; Ouyang, S.; Umezawa, N.; Cao, J.; Ye, J. *J. Am. Chem. Soc.* **2011**, *133* (17), 6490.
- (20) Royer, S.; Duprez, D.; Can, F.; Courtois, X.; Batiot-Dupeyrat, C.; Laassiri, S.; Alamdari, H. *Chem. Rev.* **2014**, *114*, 10292.
- (21) Neagu, D.; Tsekouras, G.; Miller, D. N.; Ménard, H.; Irvine, J. T. S. *Nat. Chem.* **2013**, *5*, 916.
- (22) Huang, K.; Chu, X.; Yuan, L.; Feng, W.; Wu, X.; Wang, X.; Feng, S. *Chem. Commun.* **2014**, *50*, 9200.
- (23) Huang, K.; Yuan, L.; Feng, S. *Inorg. Chem. Front.* **2015**, *2* (11), 965.
- (24) Wang, W.; Li, G.; Bai, Y.; Yang, N.; Zhang, W. *J. Phys. Chem. Solids* **2011**, *72*, 1457.
- (25) Chen, W.; Kuang, Q.; Xie, Z. *Sci. China Mater.* **2015**, *58*, 281.
- (26) Dong, L.; Shi, H.; Cheng, K.; Wang, Q.; Weng, W.; Han, W. *Nano Res.* **2014**, *798* (7), 1311.
- (27) Zhan, H.; Yang, X.; Wang, C.; Chen, J.; Wen, Y.; Liang, C.; Greer, H. F.; Wu, M.; Zhou, W. *Cryst. Growth Des.* **2012**, *12*, 1247.
- (28) Dang, F.; Mimura, K.; Kato, K.; Imai, H.; Wada, S.; Haneda, H.; Kuwabara, M. *Nanoscale* **2012**, *4*, 1344.
- (29) Lu, Z.; Tang, Y.; Chen, L.; Li, Y. *J. Cryst. Growth* **2004**, *266*, 539.
- (30) Wang, S.; Huang, K.; Hou, C.; Yuan, L.; Wu, X.; Lu, D. *Dalton Trans.* **2015**, *44*, 17201.
- (31) Yuan, L.; Huang, K.; Hou, C.; Feng, W.; Wang, S.; Zhou, C.; Feng, S. *New J. Chem.* **2014**, *38*, 1168.
- (32) Liu, B.; Hu, B.; Du, Z. *Chem. Commun.* **2011**, *47*, 8166.
- (33) Yang, X.; Xu, G.; Ren, Z.; Wei, X.; Chao, C.; Gong, S.; Shen, G.; Han, G. *CrystEngComm* **2014**, *16*, 4176.
- (34) Fei, L.; Yuan, J.; Hu, Y.; Wu, C.; Wang, J.; Wang, Y. *Cryst. Growth Des.* **2011**, *11* (4), 1049.
- (35) Li, L.; Wang, X.; Lan, Y.; Gu, W.; Zhang, S. *Ind. Eng. Chem. Res.* **2013**, *52* (26), 9130.
- (36) Siemons, M.; Leifert, A.; Simon, U. *Adv. Funct. Mater.* **2007**, *17*, 2189.
- (37) Tokunaga, Y.; Furukawa, N.; Sakai, H.; Taguchi, Y.; Arima, T.; Tokura, Y. *Nat. Mater.* **2009**, *8*, 558.
- (38) Feng, J.; Liu, T.; Xu, Y.; Zhao, J.; He, Y. *Ceram. Int.* **2011**, *37*, 1203.
- (39) Berchmans, L. J.; Sindhu, R.; Angappan, S.; Augustin, C. O. *J. Mater. Process. Technol.* **2008**, *207*, 301.
- (40) Racu, A. V.; Ursu, D. H.; Kuliukova, O. V.; Logofatu, C.; Leca, A.; Miclau, M. *Mater. Lett.* **2015**, *140*, 107.
- (41) Cheng, Z. X.; Shen, H.; Xu, J. Y.; Liu, P.; Zhang, S. J.; Wang, J. L.; Wang, X. L.; Dou, S. X. *J. Appl. Phys.* **2012**, *111*, 034103.
- (42) Hou, C.; Feng, W.; Yuan, L.; Huang, K.; Feng, S. *CrystEngComm* **2014**, *16*, 2874.
- (43) Huang, K.; Feng, W.; Yuan, L.; Zhang, J.; Chu, X.; Hou, C.; Wu, X.; Feng, S. *CrystEngComm* **2014**, *16*, 9842.
- (44) Zheng, W.; Liu, R.; Peng, D.; Meng, G. *Mater. Lett.* **2000**, *43*, 19.
- (45) Zhou, Z.; Guo, L.; Yang, H.; Liu, Q.; Ye, F. *J. Alloys Compd.* **2014**, *583*, 21.
- (46) Modeshia, D. R.; Walton, R. I. *Chem. Soc. Rev.* **2010**, *39*, 4303.
- (47) Geng, F.; Matsushita, Y.; Ma, R.; Xin, H.; Tanaka, M.; Iyi, N.; Sasaki, T. *Inorg. Chem.* **2009**, *48*, 6724.
- (48) Lee, J.-H.; Jeong, Y. K.; Park, J. H.; Oak, M.-A.; Jang, H. M.; Son, J. Y.; Scott, J. F. *Phys. Rev. Lett.* **2011**, *107*, 117201.
- (49) Wang, Y.; Yan, X.; Chen, J.; Deng, J.; Yu, R.; Xing, X. *CrystEngComm* **2014**, *16*, 858.
- (50) Zhou, M.; Yang, H.; Xian, T.; Ma, J. Y.; Zhang, H. M.; Feng, W. J.; Wei, Z. Q.; Jiang, J. L. *J. Alloys Compd.* **2014**, *617*, 855.
- (51) Selbach, S. M.; Tybell, T.; Einarsrud, M.-A.; Grande, T. *Chem. Mater.* **2007**, *19*, 6478.
- (52) Das, R.; Poddar, P. J. *Phys. Chem. C* **2014**, *118*, 13268.
- (53) Geller, S.; Wood, E. A. *Acta Crystallogr.* **1956**, *9*, 563.
- (54) Judin, V. M.; Sherman, A. B.; Myl'nikova, I. E. *Phys. Lett.* **1966**, *22*, 554.
- (55) Wu, A.; Shen, H.; Xu, J.; Wang, Z.; Jiang, L.; Luo, L.; Yuan, S.; Cao, S.; Zhang, H. *Bull. Mater. Sci.* **2012**, *35*, 259.
- (56) Hahn, S. E.; Podlesnyak, A. A.; Ehlers, G.; Granroth, G. E.; Fishman, R. S.; Kolesnikov, A. I.; Pomjakushina, E.; Conder, K. *Phys. Rev. B: Condens. Matter Mater. Phys.* **2014**, *89*, 014420.